SELECTION OF SALIENT MORPHOLOGICAL AND NETWORK FEATURES FOR
COMPUTATIONAL DIAGNOSIS OF MYOSITIS

By

MASON MCGOUGH

A THESIS PRESENTED TO THE GRADUATE SCHOOL
OF THE UNIVERSITY OF FLORIDA IN PARTIAL FULFILLMENT
OF THE REQUIREMENTS FOR THE DEGREE OF
MASTER OF SCIENCE

UNIVERSITY OF FLORIDA

2016

To my family for their continuing support

ACKNOWLEDGMENTS

TABLE OF CONTENTS

LIST OF TABLES

LIST OF FIGURES

LIST OF ABBREVIATIONS

Computer-Aided Diagnosis (CAD)	The use of imaging, informatics, and computer technology to assist doctors with diagnosis.
Convolutional Neural Network (CNN)	A supervised type of neural network architecture that applies learned filters to signals, such as images, to predict a classification on new images.
Dermatomyositis (DM)	A type of myositis characterized by muscle weakness and rashes. The pattern of inflammation is focused in the perimysial regions of muscle tissue.
Gradient Vector Flow (GVF)	A force applied to certain types of deformable models, such as snakes, that aids convergence in noisy images.
Hematoxylin and Eosin (HE)	A principal immunohistochemical stain. In muscle tissue, it stains the nuclei and inflammatory cells deep violet and the muscle cytoplasm warm pink.
Idiopathic Inflammatory Myopathy (IIM)	A set of rare heterogeneous diseases, often referred to as "myositis," that are characterized by attack of the skeletal muscle by immune cells. This set of diseases includes dermatomyositis, polymyositis, and inclusion body myositis. Myositis is most effectively diagnosed by pathologists using muscle biopsies.
Inclusion Body Myositis (IBM)	A type of myositis characterized by slow degeneration in distal and proximal muscle strength. The formation of rimmed vacuoles on muscle fibers is a hallmark of this type of myositis.
Polymyositis (PM)	A type of myositis characterized by pain and loss of proximal muscle mass. The pattern of inflammation is focused in the endomysial regions of muscle tissue.
Support Vector Machine (SVM)	A supervised learning algorithm that attempts to find an optimum decision boundary between two classes of data by identifying a subset of training points that most precisely define the boundary.
Ultrametric Contour Map (UCM)	A hierarchical representation of an image segmentation that, when different thresholds are applied, produces sets of curves with unique segmentations.
Whole-Slide Image (WSI)	A digital image file depicting a muscle tissue slide in its entirety.

Abstract of Thesis Presented to the Graduate School
of the University of Florida in Partial Fulfillment of the
Requirements for the Degree of Master of Science

SELECTION OF SALIENT MORPHOLOGICAL AND NETWORK FEATURES FOR
COMPUTATIONAL DIAGNOSIS OF MYOSITIS

By

Mason McGough

December 2016

Chair: Lin Yang
Major: Biomedical Engineering

Dermatomyositis and polymyositis are debilitating forms of myositis that rapidly inflict muscular weakness, atrophy, and rashes in patients. Differential diagnosis from muscle biopsies is a challenging subjective process that relies on studying differences in the morphological patterns of myofibers, inflammatory cells, and connective tissue. We develop a partially automated system to detect inflammatory cells, myofibers, and perimysium tissue from muscle biopsies prepared with hematoxylin and eosin staining. With a database of 56 muscle biopsy images, we analyze 900 features tailored to describe the biopsy features that practicing pathologists rely on and determine which are the most reliable for diagnosis. We obtain 90.9% accuracy by applying linear SVM classification on a cohort of held-out test slides. Of the computed features inspired by current myositis research, the most reliable features described perifascicular atrophy, or the shrinkage of myofiber size with decreasing distance from perimysium connective tissue. The detection, segmentation, and feature extraction methods here facilitate the interpretation of morphological information contained in muscle biopsies, potentially improving the quality of myositis diagnosis and accelerating the rate of muscle histology research.

CHAPTER 1
INTRODUCTION

The idiopathic inflammatory myopathies (IIM) are a set of rare heterogeneous diseases that inflict extreme muscular weakness, pain, rashes, calcinosis, and potentially deadly heart and lung complications. These diseases are chronic forms of muscle inflammation, or myositis, whose symptoms can manifest over the course of as little as several weeks. Though chiefly thought of as an affliction of the skeletal muscle, IIM also cause complications of the interstitial tissue, resulting in interstitial lung disease, arthralgia, and Raynaud's disease [1]. On occasion, myositis even presents paraneoplastic behavior, substantiating the findings that suggest a correlation between myositis and cancer development [2, 3].

The reliable differential diagnosis of the three primary subsets of chronic myositis, namely dermatomyositis (DM), inclusion body myositis (IBM), and polymyositis (PM), is a central concern for pathologists, as targeted immunotherapy measures run a significant risk of potential toxicity. Muscle biopsies are widely considered the "gold standard" with regard to reliable diagnosis, as whole-slide images (WSI) of skeletal muscle cross-sections stained with hematoxylin and eosin (HE) depict clear morphological abnormalities that distinguish myositis from unafflicted tissue. Nonetheless, many of the traditional histological features favored by pathologists are neither consistent in appearance nor exclusive to one myositis and may even overlap with muscular disorders, in particular the muscular dystrophies [4].

By employing machine learning and computer vision algorithms on medical images, computer-aided diagnosis (CAD) systems are capable of uncovering novel, clinically relevant features that have previously evaded discovery [5-12]. For instance,

with a thorough, accurate segmentation of muscle fibers from a muscle biopsy, one can

calculate the area, perimeter, min/max Feret diameters, average color, etc. of every

detected muscle fiber in the image. Such techniques mitigate the time consumed

measuring these features by hand while improving the accuracy and throughput of

measurements, all potentially invaluable improvements to current practices in muscle

biopsy research.

There is a modest body of studies that employ detection and segmentation

strategies to muscle fibers [13-21], nuclei [13, 15, 22], and perimysium [23] in skeletal

muscle images. Robust ellipse fitting followed by mean-shift segmentation is employed

to segment myonuclei and muscle fibers in one study [13]. Although effective, the

method is applied only to z-stack images, wherein nuclei have much stronger contrast

with the background than in HE images. In another study [15], myofiber type, cross-

sectional area, and myonuclear content are computed via an eigendecomposition of the

Hessian matrix and a deformable model. This method relies on fluorescence staining,

which grants both high contrast and channel separation between the bands of excitation

and thus greatly facilitates the identification of myonuclei and the dystrophin boundary

of muscle fibers. Several methods rely on fluorescence staining since it facilitates

semantic segmentation of myofibers and myonuclei [15, 17, 18, 20], but the

identification of many features associated with myositis, such as necrosis and

regeneration, is not possible in this domain. Myofiber segmentation in healthy skeletal

muscle samples is commonly addressed using deformable models [14, 16].

Segmentation of muscle fibers in HE images using texton histogram-based seed

detection and gradient vector flow (GVF) deformable model yields high agreement with

11

manual segmentation for samples with relatively normal appearance [14]. Since its evolution is driven by internal and local image-based forces, the deformable model in practice is highly susceptible to noise and convergence tends to fail for tissues in varying states of necrosis. In the case of diseased skeletal muscle, insensitivity to local distortions and degradation of myofiber boundaries demands a robust hierarchical approach and domain-specific training. In a recent study [21], this is accomplished by using a structured random forest-based edge detection to pass a small, diverse ensemble of segmentation candidates to an ultrametric contour map (UCM) for region merging.

To our knowledge, there are no studies of skeletal muscle images that utilize CAD systems to make automated diagnostic decisions regarding myositis. We developed a multi-stage system depicted in Figure 1-1 to detect and segment the salient components of a muscle biopsy, compute a multitude of descriptive features from its components, and predict whether the sample came from a DM or PM case, all while exclusively restricting the scope of our study to HE images. Muscle fibers are segmented by the state-of-the-art structured random forest and UCM muscle segmentation algorithm [21]. Inflammatory cells and myonuclei are detected by a convolutional neural network with a structured regression layer that has been demonstrated to be an effective general cell detection method for a variety of cell types, stains, and imaging modalities [24]. To facilitate the computation of several graph features, a network is constructed by connecting adjacent muscle fibers [17]. The 240 features we compute are based off of diagnostic criteria recommended by pathologists for myositis classification and are unique contributions of this study. Diagnosis is

compared using the logistic regression, linear SVM, and random forest classifiers on a

subset of the computed features selected by confidence interval. Although the system is

not entirely automated, we make several recommendations for future studies that could

push the system towards full automation.
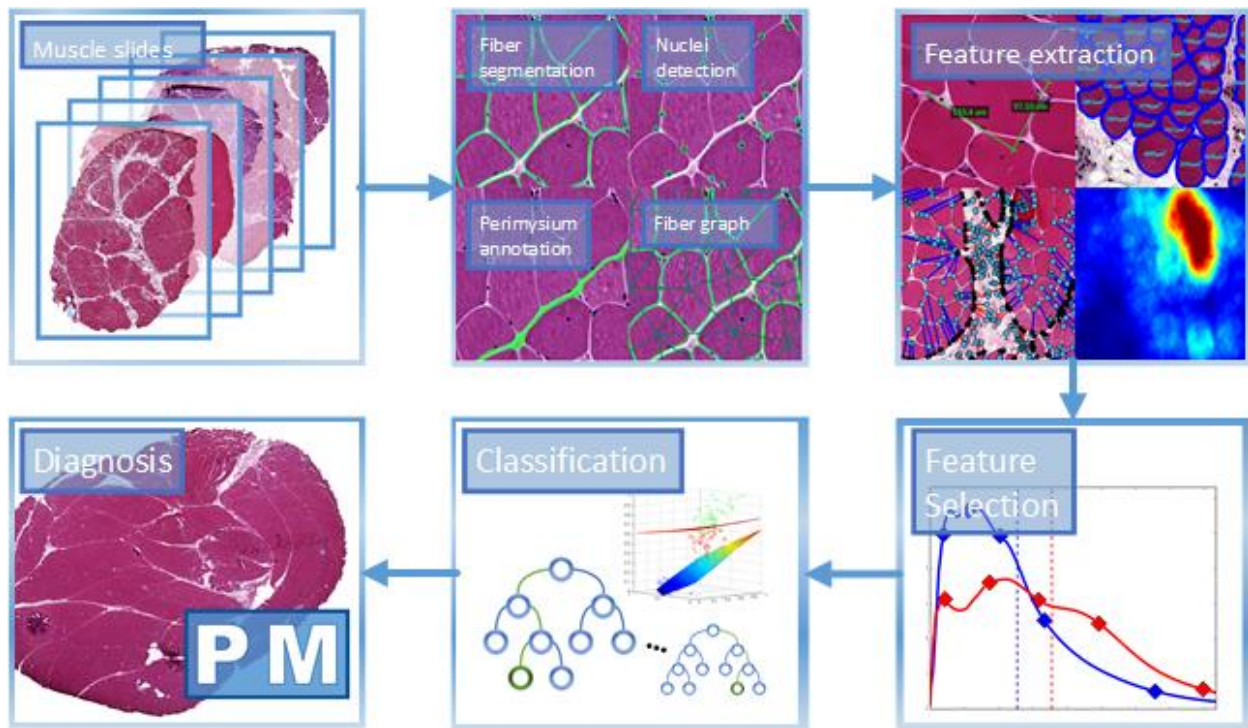
Figure 1-1. Detection, segmentation, feature extraction, and diagnosis of a muscle biopsy image. Flowchart depicting the process used in our study. Various histological components of muscle tissue relevant to the diagnosis of myositis are first detected and segmented from the raw images. A wealth of features is computed from their morphometric and distribution characteristics. The strongest features for myositis prediction are determined using feature selection. Finally, a classifier is constructed to make predictions on novel muscle biopsy images.

CHAPTER 2
METHODS

Population and Materials

The study cohort comprised of 56 individuals with whole-slide images of unique skeletal tissue samples (25 DM cases and 31 PM cases) that have been prepared with HE staining. Biopsies were obtained under local anaesthetic from the vastus lateralis muscles of patients using a 5-mm biopsy needle and manual suction. Fifty-two of these samples were prepared by the Medical College of Wisconsin Neuromuscular Laboratory (MCWNL) on a Hamamatsu NanoZoomer while the other four were prepared by the University of Kentucky Department of Molecular and Cellular Biochemistry (UKDMCB) on an Olympus Virtual Slide Microscope. The raw images were captured on a 40X objective and analyzed at 13X magnification. With the exception of the pathologist diagnosis, the images were provided with no clinical, molecular, biochemical, genetic, or personally-identifiable information that might aid in diagnosis. Any potentially informative clinical data was deliberately omitted. Eleven (5 DM and 6 PM) of these 56 images were set aside as testing data.

Detection and Segmentation

Muscle biopsies, transverse cuts of histological stained skeletal muscle, are the tool of choice for pathologists aiming to differentially diagnose DM and PM in a potentially afflicted patient. Any muscle biopsy slide depicts a structured arrangement of muscle fibers, or myocytes, fastened into bundles called fascicles by a connective tissue called endomysium and encircled by a larger-scale network of connective tissue called perimysium, depicted in Figure 2-1. Biopsies from a patient with an autoimmune myopathy frequently exhibit an alarming density of myonuclei and inflammatory cells,

15

henceforth generically referred to as "nuclei", scattered about the tissue. The majority of features that pathologists consider relevant for discriminating DM and PM are based on abnormalities in structure and distribution of myocytes, connective tissue, and nuclei throughout the muscle tissue. To adequately complete the computation of features from the myocytes, nuclei, and perimysium of muscle biopsies, we first isolate these components from the interstitial tissue and background using a combined detection and segmentation approach.

Myofiber Segmentation

Although methods for segmentation of myocytes have been explored frequently in the literature [13-21], they often rely on different types of staining and frequently fail when presented with myocytes that differ radically in appearance from normal tissues. Myodegenerative diseases like IIM can cause considerable changes in texture and morphology of myocytes that prevent noise-sensitive algorithms such as active contour models from converging. The difficulty in myocyte segmentation in HE images lies in the ability to distinguish true myofiber boundaries from false edges, particularly for fibers in various states of degeneration, while also making appropriate inferences in places where fiber boundaries are unclear or implied. Thus, to consistently segment myocytes using only HE staining, we require a method that utilizes contextual information while being robust to perturbations in texture and morphology.

Given a set of samples $S_i = \{x_i \in X, y_i \in Y\}$, where x_i denotes input images and y_i denotes labeled edge patches, a random forest with a structured output that produces edge predictions is trained. Decision nodes are split by maximizing the following information gain criterion:

$$\delta H(S_n) = H(S_n) - \left(\frac{|S_n^L|}{|S_n|} H(S_n^L) + \frac{|S_n^R|}{|S_n|} H(S_n^R) \right) \tag{2-1}$$

where $H(S_n)$ denotes the class entropy function, S_n^L and S_n^R denote the set of samples S_n split into left and right decisions at the decision node, respectively, and $\delta H(S_n)$ denotes the total information gain at that node. This training procedure is only applicable for binary labels, so the set of labels Y is first compressed by an autoencoder for dimensionality reduction and then clustered into edge and non-edge groups using k-means. The leaf nodes of each decision tree form their own structured outputs, which are chosen to be the median of all the labels Y passed to that node. For this experiment, a forest of 100 trees was selected.

The edge map produced by this structured random forest is then oversegmented by a modified watershed transform to produce the UCM, pictured in Figure 2-2. The watershed contour lines are weighted in the range $[0, 1]$ by the activations of the edge map filtered by second derivative of Gaussian filters at eight different, equally spaced orientations. A set of segmentation regions $V = \{v_i, i = 1, 2, \ldots n\}$ is created by thresholding the UCM at five different thresholds, specifically 0.99, 0.95, 0.90, 0.80, and 0.70. Naturally, many of these regions overlap with regions at different thresholds. Together they form a weighted tree graph where regions at one threshold may be comprised by the union of several regions at another threshold. Each region $v_i \in V$ is assigned a score $w(v_i)$ in the range $[0, 1]$ by a decision random forest indicating its similarity to a true muscle fiber. Finding the optimum set of non-overlapping regions amounts to a bottom-up dynamic programming problem. For a node vector $X \in \{0, 1\}^n$ indicating whether or not the node has been selected, this problem is formulated as:

17

$$X^* = \arg\max_x w^T X, s.t. x_i + x_j \leq 1, if\ a_{ij} = 1 \qquad (2\text{-}2)$$

where w is the vector of scores corresponding to regions in the set V and the node vector X^* indicates the X corresponding to the optimal set of selected nodes according to the scores w.

Myonuclei Detection

Convolutional neural networks (CNN) are among the most sophisticated, yet robust state-of-the-art methods for object detection in both natural and cell histopathology images [26-29]. Their unparalleled performance in detection and segmentation tasks is only stymied by the slow and unpredictable convergence of their model parameters during training, which is best addressed with massive, diverse training sets. This typically presents a particular challenge for histology tasks, as obtaining large amounts of training data is complicated by privacy regulations and the labor needed of pathologists to provide reliable annotations. The structured regression CNN model can nonetheless be successfully trained and employed for detection in histology images by taking advantage of several data manipulation techniques [22]. In this study, we employ the same network architecture as that described in the original paper.

To train the network to identify nuclei in this particular domain of HE-stained muscle biopsies, we crop images from 12 of the most visually diverse WSI in the MCWNL data set. The nuclei in each image are annotated manually by first applying an initial detection with color thresholding and then fine-tuning with a MATLAB graphical user interface that allows for the easy manipulation of coordinates on an image by simple point-and-click operations. From this set of images with a list of centroids

corresponding to nuclei locations, a ground truth regression for the training image is produced according to the following heuristic:

$$M_{ij} = \begin{cases} \dfrac{1}{1 + \alpha D(i,j)} & if\ D(i,j) \leq r \\ 0 & otherwise \end{cases} \tag{2-3}$$

Where M_{ij} indicates the regression level at position (i,j) within the regression image, $D(i,j)$ is the Euclidean distance of point (i,j) from a centroid, r is a threshold radius, and α is some decay ratio. For our experiments, r and α were set to 8 and 0.5, respectively. Next, small 40 x 40 crops centered around each centroid are extracted from the original RGB images to use as inputs, with corresponding 10 x 10 crops extracted from the same location in the regression image to use as outputs. The number of unique regression crops is artificially increased by rotating and mirroring the crops. The network is then trained from these pairs of input-output patches via backpropagation by solving the following optimization problem with respect to the network parameters θ_L:

$$\arg \min_{\theta_1,\ldots,\theta_L} \frac{1}{N} \sum_{i=1}^{N} \frac{1}{2} \left\| \left(Diag(y^i) + \lambda I\right)^{\frac{1}{2}} (y^i - o^i) \right\|_2^2 \tag{2-4}$$

Where y^i denotes the columnar form of the regression patch of sample image patch i, o^i denotes the regression output of the network for input patch i, $Diag(y^i)$ represents the diagonal matrix form of column vector y^i, and λ reweighs the nonzero regions of the image patch to increase their loss and mitigate poor convergence. The loss function was optimized using stochastic gradient descent with a batch size of 128 crops, a learning rate of 0.001, and a fine momentum of 0.8. This network configuration utilizes the fast scanning technique [30] to rapidly produce a structured regression of

proximity estimates across the entire image. We then convert the proximity map to a set of coordinates corresponding to nuclei detections by searching for local maxima.

Feature Extraction

Pathologists have described a number of biopsy-based diagnostic features related to DM or PM [31] that are characterized by the appearance, shape, and distribution of myofibers, nuclei, and perimysium, depicted in Figure 2-3. Inflammation in DM, for instance, is particularly confined to the perimysial and perivascular regions, seen in Figure 2-3a. This feature, called perimysial/perivascular inflammatory cell infiltrate, is a key feature of DM and is directly characterized by the distribution of nuclei with respect to the perimysium region. This distinct infiltration pattern is often accompanied by a regular decrease in myofiber size and rounding of shape along the perimysium regions known as perifascicular atrophy, seen in Figure 2-3c. On the other hand, endomysial inflammatory cell infiltrate is a pattern of inflammation characteristic of PM that manifests in localized clusters among the endomysium between myocytes, as seen in Figure 2-3b. Abnormal aggregation of inflammatory cells in the perimysium regions may still be present in PM cases, but it is rarely accompanied by perifascicular atrophy. Myonecrosis and regeneration of fibers, depicted in Figure 2-3e, occurs differentially in DM and PM cases, although it is particularly associated with DM and may give way to visible differences in shape and color of myofibers. Endomysial fibrosis (the widening of the endomysial regions), scattered muscle fiber hypertrophy, myophagocytosis (the appearance of many nuclei within muscle fibers as a result of macrophages clearing cellular debris), attack of autoaggressive lymphocytes in nonnecrotic myofibers (Figure 2-3d), and the presence of scattered angular atrophic muscle fibers (muscle fibers that are shrunken to highly sharp and nonconvex shapes,

20

Figure 2-3f) are all features that tend to be more prominent in cases of PM than DM but may be present to varying degrees in both forms of myositis.

Although a wealth of sophisticated feature decomposition and feature learning methods have facilitated feature extraction for general data analysis problems, our study is partly intended as a proof of concept for further research into the morphology of skeletal muscle. As such, we opted to include only hand-crafted features with clear semantic meaning for this experiment. We compute a broad variety of features from the appearance, shape, and spatial relationship of these three histological components, including basic features like the area, perimeter, compactness, and major and minor axis lengths of myofibers. We fit an active shape model [32] across a subset of the detected myofibers, keeping the eigenvectors that explain 98% of the variance of the data and using their sparse coefficients as features. Since the distribution of nuclei throughout the perimysium and endomysium is a highly discriminative marker for pathologists, we collect the distance of every detected nucleus from both the nearest perimysium edge and the nearest myofiber edge as well as compute a kernel density estimation of nuclei across both perimysium and non-perimysium regions.

Network theory is beginning to be applied to histology images in order to uncover higher-order patterns of organization in cellular systems. In one instance, researchers found that they could successfully discriminate between epithelial samples of different organisms and even between different types of epithelia within the same organism entirely with network features [12]. Many of our features stem from a graph that treats adjacent myofibers as connected nodes by using a variation on a method for muscle network analysis [17]. This graph enables the description of local variation in features of

a myofiber with its connected neighbors, such as the standard deviation of myofiber area with its neighbors. It also allows for the modeling of the magnitude and direction of intensity change of a feature with respect to its neighbors. For a given feature and node, each neighbor of the node is assigned a Euclidean vector centered on the node's centroid. The magnitude of each vector is proportional to the magnitude of the current feature corresponding to that neighbor. The angle of each vector is given by the angle of the edge connecting the current node's centroid to the neighbor's centroid. The gradient of that feature at a given myofiber node is given by the mean vector of its neighbors. Figure 2-4 illustrates the construction of these gradient features for a given myofiber node. In concept, this feature should capture the direction and intensity of local change of a feature with respect to its neighbors, such as gradual shrinking of myofibers along a given direction. We use both the magnitude and angle of the gradient of every myofiber feature as features. We also use the standard deviation of these features with the neighbors of a node as features. Including these muscle graph features, we analyze a total of 240 features.

Presentation of histological features has a high natural variance throughout the body, particularly if steroid treatment has already begun. Even with MRI prescreening to aid in selecting regions with high probability of displaying diagnostically relevant histological features [33], it is common to find that features like perifascicular atrophy and inflammatory cell infiltrate are irregularly distributed throughout the muscle sample, with many regions showing no evidence of such features. The distribution of most of these relevant features throughout the muscle tissue is highly nonstationary, so simply taking the mean of each feature over the whole slide will not suffice. We instead

calculate the 5th, 25th, 50th, 75th, and 95th percentile values of that feature for each slide. This method much more accurately characterizes the true distribution of the data, is more robust to outliers without discarding the information that they carry, and does not assume a normal distribution. The nuclei density features are described over regions of the entire slide, not over discrete observations, and so they are excluded from this percentile calculation. By applying this approach to all included features, a total of 900 features is produced.

Feature Selection and Classification

Since the features we use are comprised of measurements regarding muscle fibers, nuclei, and perimysium, the number of finite observations between different features differs greatly. This precludes the use of hypothesis tests, which have a well-known scale effect on their p-values [24], as a means of univariate feature selection. Instead, we generate two confidence intervals at 95% confidence from the DM and PM subsets of the data. We then select the features whose DM and PM confidence intervals do not overlap. However, the confidence interval method does not provide a way to evaluate the relative predictive strength of our features for the task of DM vs. PM delineation. Note that because of our feature resampling method, we are left with exactly five observations per feature per slide. This, via the Central Limit Theorem, enables us to use p-values derived from the Welch's t-test of unequal variances to evaluate and compare the independent predictive strength of selected features.

Once we have narrowed down our list of features to a subset with predictive strength, we wish to train a classifier to make robust diagnostic predictions on new WSI using these features. To solve categorical classification problems, it is common practice to resort to one of the many supervised learning algorithms for making inferences on

numerical data. The feature subset is validated empirically using the L1-regularized logistic regression, linear support vector machine (SVM), and random forest classifiers. The C constant of linear SVM was determined by a fine grid search and five-fold cross-validation. The number of trees in the random forest was set to 100. We then report the final accuracy, sensitivity, and specificity of each algorithm as the averaged predictions over the test set.
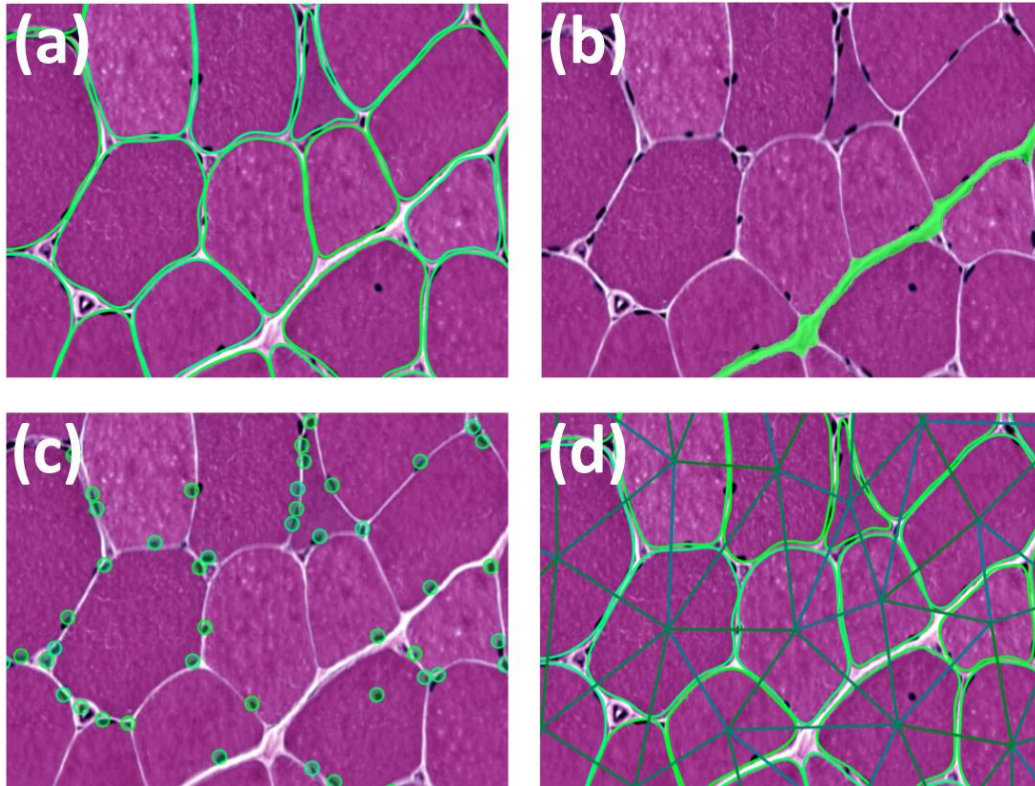
Figure 2-1. Components of a muscle biopsy. The components of a muscle biopsy detected and segmented by our model. (a) Myofibers, or muscle fibers. (b) Perimysium, the connective tissue that sheathes large bundles of myofibers. (c) Myonuclei and inflammatory cells, seen as small basophilic structures scattered throughout the muscle tissue. (d) Myofiber graph, formed by treating myofibers as nodes and connecting them to adjacent myofibers.

Figure 2-2. Hierarchical image segmentation via UCM. Steps of our adaptation of the contour detection and hierarchical image segmentation method [25]. (a) The original muscle image. (b) The edge map following the structured random forest edge detection. (c) The weighted set of oriented watershed edges as input to the UCM. (d) The final segmented contours.
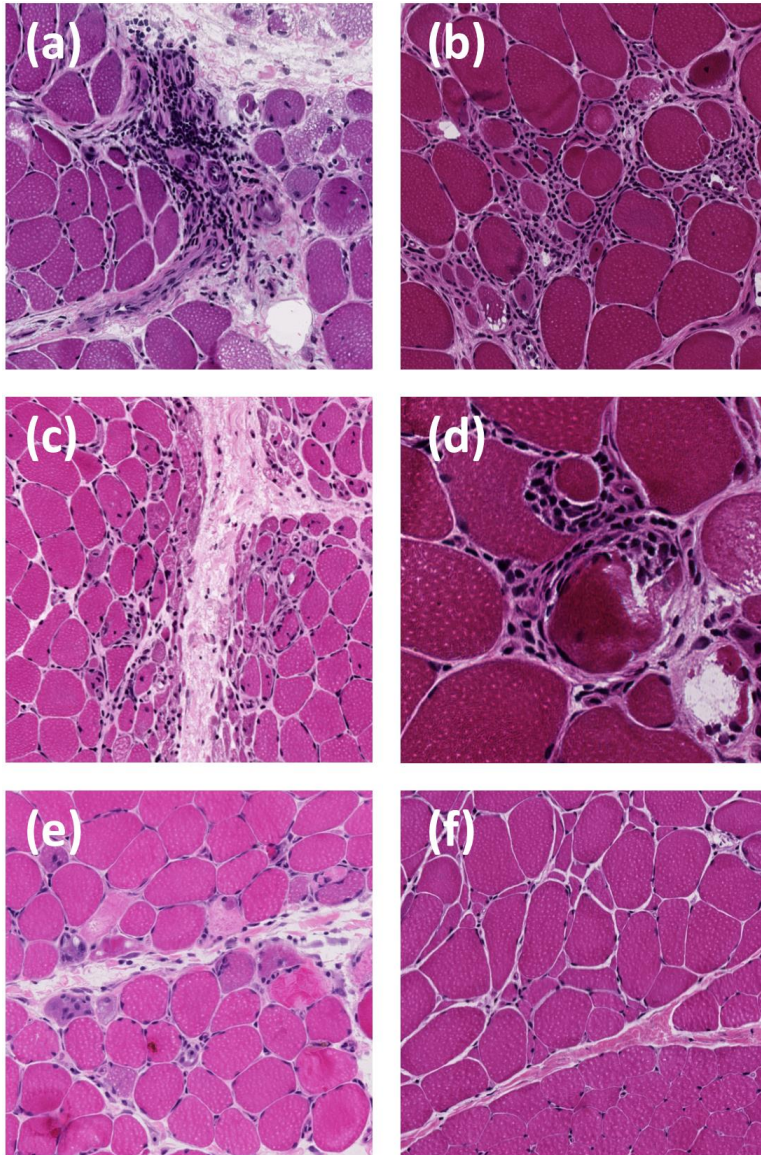
Figure 2-3. Pathology features for myositis diagnosis. Several biopsy features strongly associated with either DM or PM. (a) Perimysial inflammatory cell i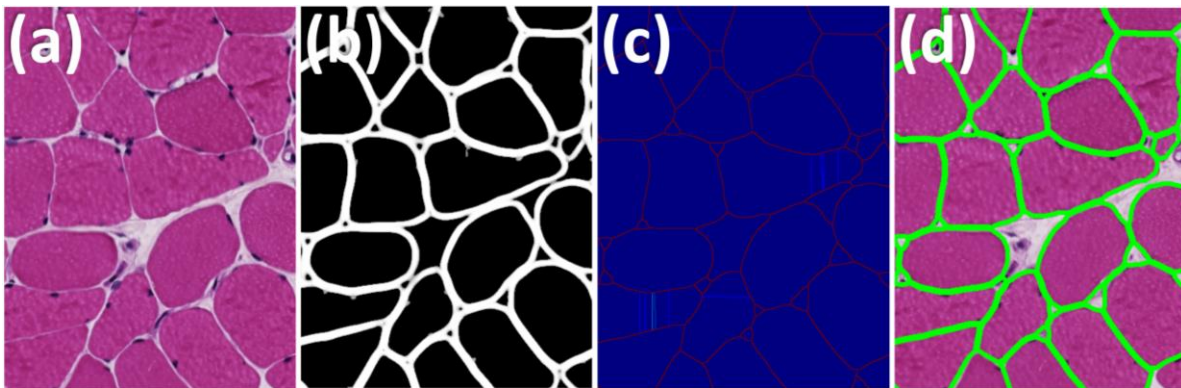nfiltrate: aberrant infiltration of inflammatory cells in regions of the perimysium. (b) Endomysial inflammatory cell infiltrate: clusters of inflammatory cell infiltration in regions of the endomysium, without regard to proximity to perimysium. (c) Perifascicular atrophy: increasing shrinkage of myocytes as distance to nearby perimysium decreases. (d) Autoaggressive lymphocyte attack: nonnecrotic fibers with invaginations and T-lymphocyte infiltration. It is thought to be implicated in the pathogenesis of PM. (e) Necrosis and regeneration: death and regrowth of myocytes throughout tissue, accompanied by relative changes in cytoplasm color to light pink and purple, respectively. (f) Angular atrophy: change in the convex, polygonal shape of normal myofibers to sharp, sometimes nonconvex, and atrophied cells. It occurs without respect to perimysium.
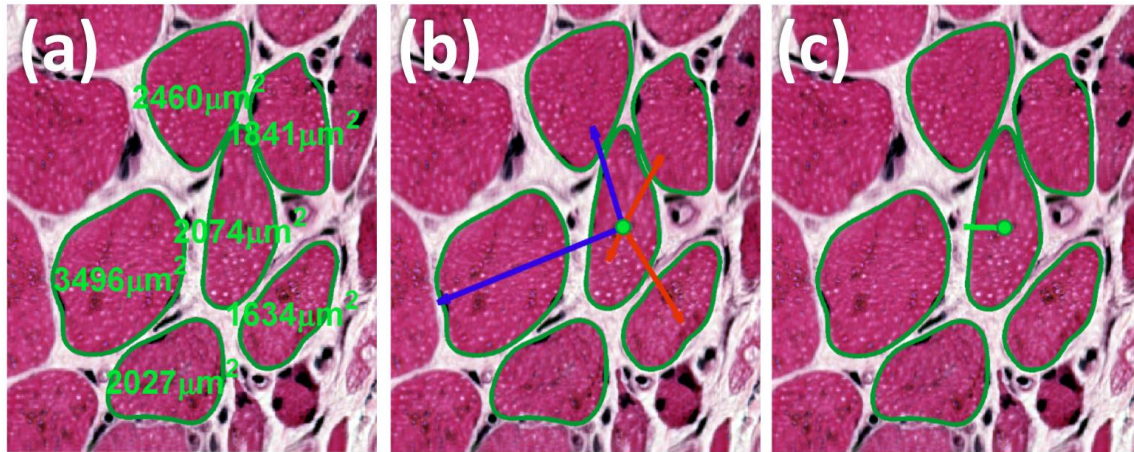
Figure 2-4. Construction of myofiber gradient features. (a) A node myofiber is surrounded by its neighbors. The myofiber area feature is pictured in green (μm^2). (b) Each neighbor of the node is assigned a vector centered on the node's centroid. The magnitude of this vector is proportional to the difference in value of the current feature between the neighbor and node. Blue arrows indicate a positive difference whereas red arrows indicate a negative difference. In this example, the vectors of neighbors with greater area are blue and the vectors of neighbors with lesser area are red, with arrow length indicating the magnitude of this difference. The angle of the vector is equal to that of the edge connecting the node and the neighbor centroids. (c) The resulting feature gradient for the node is the mean vector of all neighbors.

CHAPTER 3
RESULTS

At its core, our detection and segmentation system has the capacity for more than simply diagnosing DM and PM tissues: it establishes a template for rapidly extracting morphological information from any HE-stained muscle biopsy images. Even before the feature selection and classification stages, the feature extractor is capable of providing useful analytics about the appearance and distribution of myofibers, nuclei, and perimysium within muscle specimens under study, even for pathologies such as DM that coincide with significant alterations to the morphology of the tissue. The relatively large pool of features before selection in fact provides a wealth of information regarding the degree and distribution of certain features with respect to the DM and PM subsets of myositis.

Table 3-1 depicts several examples of such analytics for a subset of the features, like myofiber area, myonuclei count, and minimum and maximum Feret diameter. Mean myofiber area for both DM (3,048 μm^2) and PM (4,106 μm^2) is much lower than the mean reported in the literature [16] for normal tissue (5,625 μm^2). This can be attributed to the muscle atrophy that often accompanies myositis, specifically perifascicular atrophy in DM cases and angular atrophy in PM cases. Hypertrophy of myofibers can also accompany atrophy, as healthy myofibers struggle to compensate for the strength lost due to atrophy of adjacent muscle fibers. The 95th percentile of PM cases is 8,001 μm^2, possibly indicating the presence of sporadic hypertrophy. As is the case with myofiber area, the averages for minimum Feret diameter, maximum Feret diameter, and perimeter are all lower in DM as opposed to PM, as expected. Perhaps surprising is that

the standard deviation is also smaller despite the lower number of DM myofibers, suggesting that fiber size variation is typically larger in PM than in DM.

Each detected myofiber in a muscle sample is connected to the adjacent myofibers as nodes in a graph. The "node standard deviation of area" feature describes the standard deviation of the area of a myofiber and all of its neighbors in the graph. Higher values of this feature thus indicate greater size variation in size of adjacent myofibers. The mean of this feature is higher overall for PM than it is in DM, which agrees with our intuition about the types of atrophy involved; perifascicular atrophy gradates in a steady fashion relative to the perimysium, as opposed to the sporadic variation in myofiber size that typifies angular atrophy.

The 56 images were completely decomposed into 900 features using the combined detection, segmentation, and feature extraction system described. Of the 900 features generated by sampling the 5th, 25th, 50th, 75th, and 95th percentiles of the original 240 features, 40 returned DM and PM confidence intervals that did not overlap. These features and their confidence intervals and p-values are listed in Table 3-2. Fiber size and appearance, nuclei distribution, and proximity of adjacent fibers are all represented by the selected features. Of these 40 features, 32 had p-values that were considered significant ($p < 0.05$). The most significant of these features is the 25th percentile of nuclei-perimysium distance ($p = 0.0002$), implying that the proportion of nuclei with relatively small distances to the perimysium regions is a strong predictive feature and recalling the perimysial inflammatory cell infiltrate feature described in the pathology literature [33]. Of particular interest is that all five percentiles of the perifascicular atrophy feature were selected as well as 14 graph features derived from

this measure, suggesting that this feature conveys the vast majority of information

regarding diagnosis between DM and PM. This agrees with conventional logic, as

perifascicular atrophy is traditionally the most critical key feature of DM [31]. It is worth

noting that these percentile features describe entire slides, meaning the degrees of

freedom for each t-test are identical. Several of these features are illustrated in Figure

3-1.

Estimations of the probability densities of several of the selected features are

depicted in Figure 3-2. Density estimations were performed over the raw training data

with respect to DM cases (blue) and PM cases (red). The percentiles of the training data

are depicted as diamond-shaped tick marks laid over the curves and the population

means are depicted as dashed lines. Most of the depicted curves are skewed quite

prominently and none are normally distributed. The percentile markers are far more

expressive of the true distribution of the data than the population means alone, at the

expense of more features. The added dimensionality is mitigated by our confidence

interval feature selection, which only selects the most reliably discriminative percentiles

from these distributions. The area feature produces a peak in the lower end of the DM

distribution, approximately around 1300 μm^2. The peak in the PM distribution is much

broader and ill-defined, since atrophy and hypertrophy are more unpredictable in PM

cases. The DM distributions of the node standard deviation of perifascicular atrophy and

node standard deviation of gradient magnitude of perifascicular atrophy features exhibit

taller and tighter peaks at lower values than the PM distributions. This perhaps indicates

that the pattern of perifascicular atrophy is more predictable in DM cases than in PM

cases. Peculiarly, the node gradient magnitude of perifascicular atrophy feature exhibits

the same pattern. In true cases of perifascicular atrophy, the change in area of

myofibers towards the perimysium region is slow and gradual. In PM cases, atrophy can

occur intensely and sporadically, either close to or far from perimysium regions. This

may explain the greater spread in the distribution of this feature with respect to PM.

As do the magnitude of myofiber gradients, it would seem likely that the angles of

myofiber gradients also carry some discriminative information. Several angle features

are depicted as polar histograms in Figure 3-3. These histograms depict the distribution

of the difference between the angle of a myofiber gradient and its neighbor myofibers.

The results are not particularly distinct, although DM cases possess noticeably less

spread around the 0° mark than PM cases. This agrees with the intuition that gradients

should be more consistent among neighbors in DM cases due to perifascicular atrophy.

Peculiarly, the IPQ compactness feature possesses the most distinct pair of polar

histograms, despite not being selected. Only one of these angle features was selected

(5th percentile of the gradient angle of perifascicular atrophy).

The accuracy, sensitivity, and specificity from training the L1-regularized logistic

regression, linear SVM, and random forest classifiers on the 11 test images are

depicted in Table 3-3. Using the 40 features selected by confidence interval, the linear

SVM (90.9% accuracy) and logistic regression (90.9%) classifiers yield the highest

accuracy followed by random forest (89.3% accuracy). Since our method relies on

manual annotation of perimysium, we also train and test these models using only the

nine features that do not require perimysium annotations, as depicted in Table 3-4. This

results in a modest decrease in accuracy for the random forest (83.9%) and slightly

higher decreases in accuracy using the linear SVM (81.8%) and logistic regression

(81.8%) classifiers.

Table 3-1. Morphological comparisons between DM and PM samples

Feature name	DM				PM			
	5%	95%	Mean	Std (σ)	5%	95%	Mean	Std (σ)
Area	387.00	6521.00	3047.48	1533.37	387.00	6521.00	3047.48	1533.37
Min Feret diameter	15.88	77.28	46.95	11.36	15.88	77.28	46.95	11.36
Max Feret diameter	29.81	117.99	74.97	18.40	29.81	117.99	74.97	18.40
Perimeter	77.56	318.30	201.42	51.03	77.56	318.30	201.42	51.03
IPQ	0.63	0.96	0.82	0.11	0.63	0.96	0.82	0.11
Perifascicular atrophy	7.40E+02	8.64E+05	1.96E+05	1.42E+05	7.40E+02	8.64E+05	1.96E+05	1.42E+05
Nuclei-perimysium distance	-33.56	259.01	66.35	30.26	-33.56	259.01	66.35	30.26
Myonuclei count	0.00	4.00	1.66	0.66	0.00	4.00	1.66	0.66
Nuclei density in perimysium	7.29E-07	2.77E-06	1.56E-06	5.63E-07	7.29E-07	2.77E-06	1.56E-06	5.63E-07
Nuclei density outside perimysium	1.16E-06	2.27E-06	1.42E-06	3.09E-07	1.16E-06	2.27E-06	1.42E-06	3.09E-07
Node std. area	350.50	2484.85	1279.91	615.38	350.50	2484.85	1279.91	615.38
Node std. min Feret diameter	5.16	22.68	13.11	3.39	5.16	22.68	13.11	3.39
Node std. max Feret diameter	6.94	31.10	17.83	5.09	6.94	31.10	17.83	5.09
Node std. perimeter	17.48	82.34	45.76	20.33	17.48	82.34	45.76	20.33
Node std. area gradient (magnitude)	154.91	1063.12	579.95	308.58	154.91	1063.12	579.95	308.58
Node std. area gradient (angle)	0.44	1.25	1.03	0.42	0.44	1.25	1.03	0.42

Table 3-2. Selected features

Feature name	DM		PM		
	CI (lower)	CI (upper)	CI (lower)	CI (upper)	p-value
(p25) Nuclei-perimysium distance	1.34	10.75	13.28	19.60	0.0002
(p5) Perifascicular atrophy	610.36	661.74	1185.72	1677.72	0.0009
(p25) Node σ perifascicular atrophy	2.13E+04	3.58E+04	6.04E+04	7.39E+04	0.0016
(p50) Node σ perifascicular atrophy	5.67E+04	6.22E+04	9.77E+04	1.46E+05	0.0017
(p25) Grad. mag. perifascicular atrophy	5.72E+04	9.99E+04	1.66E+05	2.00E+05	0.0020
(p50) Grad. mag. perifascicular atrophy	1.74E+05	1.92E+05	2.75E+05	4.37E+05	0.0021
(p25) Fiber blue skewness	0.12	0.48	0.62	0.77	0.0022
(p25) σ grad. mag. perifascicular atrophy	6.25E+04	7.48E+04	1.14E+05	1.64E+05	0.0024
(p25) Myonuclei count	0.16	0.46	0.54	0.75	0.0026
(p5) σ Grad. mag. perifascicular atrophy	1.68E+04	4.18E+04	5.37E+04	7.03E+04	0.0031
(p95) Min node endomysium eccentricity	3.57	6.14	2.58	3.12	0.0040
(p50) σ grad. mag. perifascicular atrophy	1.13E+05	1.25E+05	1.98E+05	2.69E+05	0.0047
(p75) Node σ perifascicular atrophy	1.00E+05	1.21E+05	1.60E+05	2.45E+05	0.0049
(p5) Max node perimysium eccentricity	3.97	6.92	2.92	3.64	0.0053
(p50) Perifascicular atrophy	3.31E+04	4.60E+04	9.32E+04	1.04E+05	0.0059
(p75) Grad. mag. perifascicular atrophy	3.49E+05	3.99E+05	4.61E+05	7.90E+05	0.0084
(p25) Fiber green skewness	0.69	1.05	1.07	1.83	0.0090
(p5) Fiber green kurtosis	0.02	0.03	0.04	0.06	0.0113
(p75) Perifascicular atrophy	1.56E+05	1.72E+05	2.30E+05	3.39E+05	0.0114
(p5) Fiber green skewness	0.08	0.73	0.84	1.10	0.0132
(p75) Nuclei-fiber distance	4.85	4.96	2.01	2.84	0.0138
(p75) σ grad. mag. perifascicular atrophy	1.74E+05	2.26E+05	2.86E+05	4.01E+05	0.0161
(p95) Node σ perifascicular atrophy	1.65E+05	2.59E+05	3.77E+05	4.21E+05	0.0195
(p95) Grad. mag. perifascicular atrophy	6.55E+05	9.26E+05	1.06E+06	1.53E+06	0.0230
Nuclei non-perimysium density kurtosis	1.05E-12	1.10E-12	2.81E-12	1.11E-11	0.0230

Table 3-2. Continued

Feature name	DM		PM		
	CI (lower)	CI (upper)	CI (lower)	CI (upper)	p-value
(p25) Perifascicular atrophy	2067.96	3139.09	4866.55	7001.91	0.0343
(p25) Area	928.50	1059.66	1356.66	1844.42	0.0348
(p95) Perifascicular atrophy	4.58E+05	5.63E+05	6.59E+05	9.50E+05	0.0351
Nuclei non-perimysium density σ	2.61E-13	3.68E-13	5.54E-13	1.20E-12	0.0452
(p95) σ grad. mag. perifascicular atrophy	3.40E+05	4.14E+05	5.24E+05	6.76E+05	0.0478
(p5) Area	378.28	395.94	528.81	922.38	0.1293
(p25) Min node perimysium eccentricity	1.81	2.26	1.36	1.66	0.1435
(p5) Grad. angle perifascicular atrophy	0.13	0.31	0.33	0.36	0.1612
(p5) Grad. mag. fiber-perimysium distance	5.10	6.82	7.45	10.67	0.2376
(p50) Nuclei-fiber distance	0.94	0.97	0.64	0.89	0.2698
Nuclei perimysium density σ	4.35E-13	6.35E-13	6.94E-13	7.55E-13	0.2834
(p5) Min fiber-fiber perimysium distance	1.08	1.18	0.84	0.97	0.3022
(p5) Node σ fiber-perimysium distance	2.55	3.02	3.51	4.21	0.3093

Table 3-3. Classification accuracy using 40 selected features

		DM		PM	
	Accuracy	Sensitivity	Specificity	Sensitivity	Specificity
L1-regularized logistic regression	0.9091	1.0000	0.8333	0.8333	1.0000
Linear SVM	0.9091	1.0000	0.8333	0.8333	1.0000
Random forest	0.8929	0.8846	0.9000	0.9000	0.8846

Table 3-4. Classification accuracy using 9 non-perimysium features

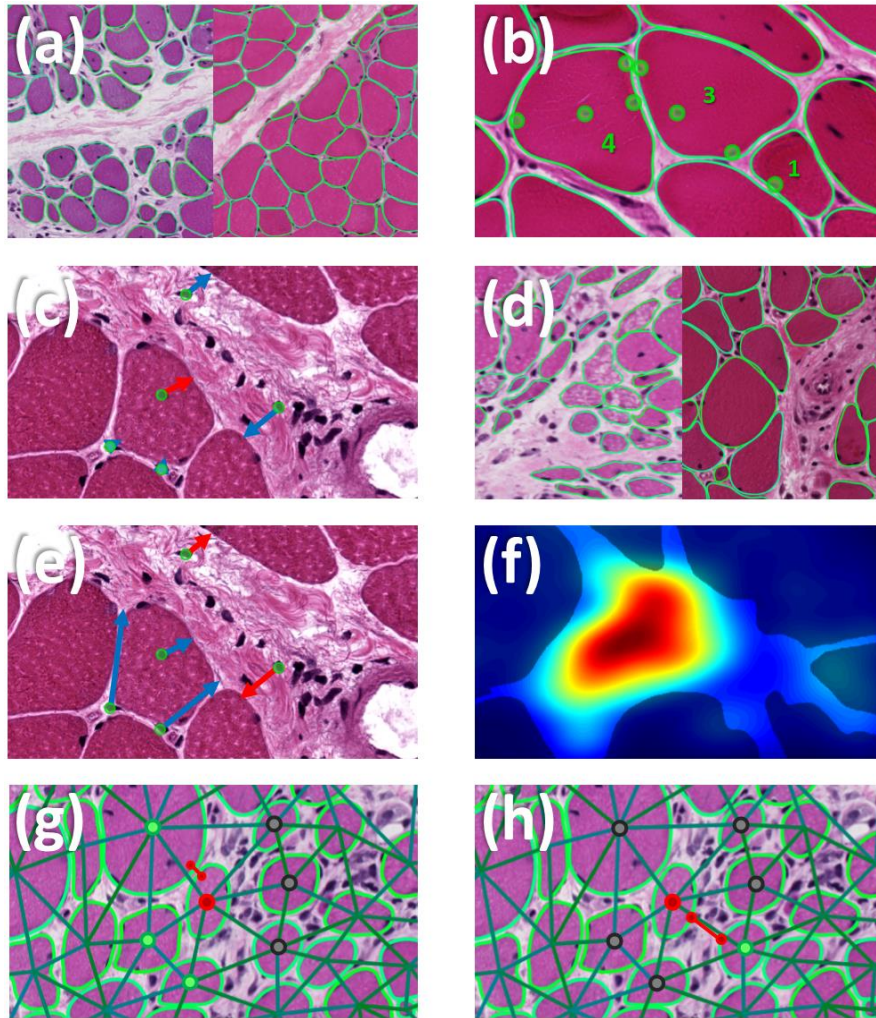|		DM		PM	
	Accuracy	Sensitivity	Specificity	Sensitivity	Specificity
L1-regularized logistic regression	0.8182	0.8000	0.8333	0.8333	0.8000
Linear SVM	0.8182	0.8000	0.8333	0.8333	0.8000
Random forest	0.8393	0.8077	0.8667	0.8667	0.8077

Figure 3-1. Several of the most predictive computed features. (a) Fiber area, in μm^2. The left and right sidescontain an average DM and PM sample, respectively. (b) Myonuclei count within a given fiber contour. (c) Nuclei-fiber distance: the distance between each detected nucleus and the nearest fiber boundary, in μm^2. Red arrows indicate negative distances. (d) Perifascicular atrophy: the product of myofiber size and the smallest Euclidean distance between its boundary and the perimysium region. The left and right sides each contain an average DM and PM sample, respectively. (e) Nuclei-perimysium distance: the distance between each detected nucleus and the nearest perimysium boundary, in μm^2. Red arrows indicate negative distances. (f) Nuclei density: the kernel density estimation of nuclei centroids over the region. (g) Min node eccentricity for endomysium-connected fibers: the minimum distance across endomysium between a node fiber and all of its endomysium-connected fibers. The red centroid indicates the current node, the green centroids indicate neighbors that are implicated in calculating the feature and the grey centroids indicate neighbors that are not used. (h) Min fiber-fiber distance across perimysium: the minimum distance between contours belonging to a given pair of adjacent fibers separated by perimysium in the fiber graph.
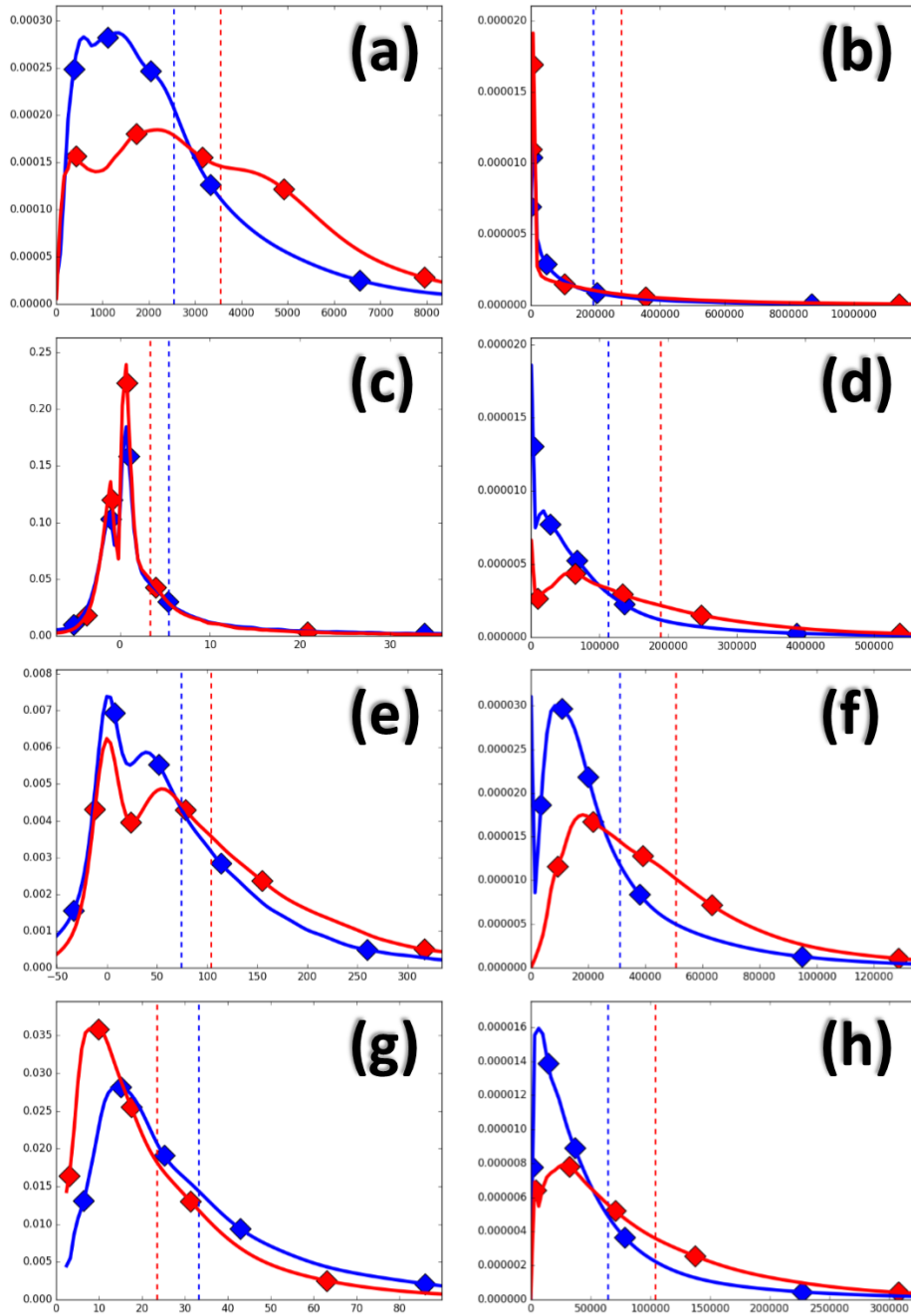
Figure 3-2. Probability distributions for several of the selected features (blue: DM, red: PM). Probability density estimations for several of the selected features. The percentiles of DM and PM are marked with diamonds. The colored dashed lines indicate the location of the respective population means. Note that these distributions were produced from performing a normal kernel density estimation over the training data. (a) Fiber area. (b) Perifascicular atrophy. (c) Nuclei-fiber distance. (d) Node standard deviation of perifascicular atrophy. (e) Nuclei-perimysium distance. (f) Node gradient magnitude of perifascicular atrophy. (g) Max node eccentricity across perimysium. (h) Node standard deviation of gradient magnitude of perifascicular atrophy.
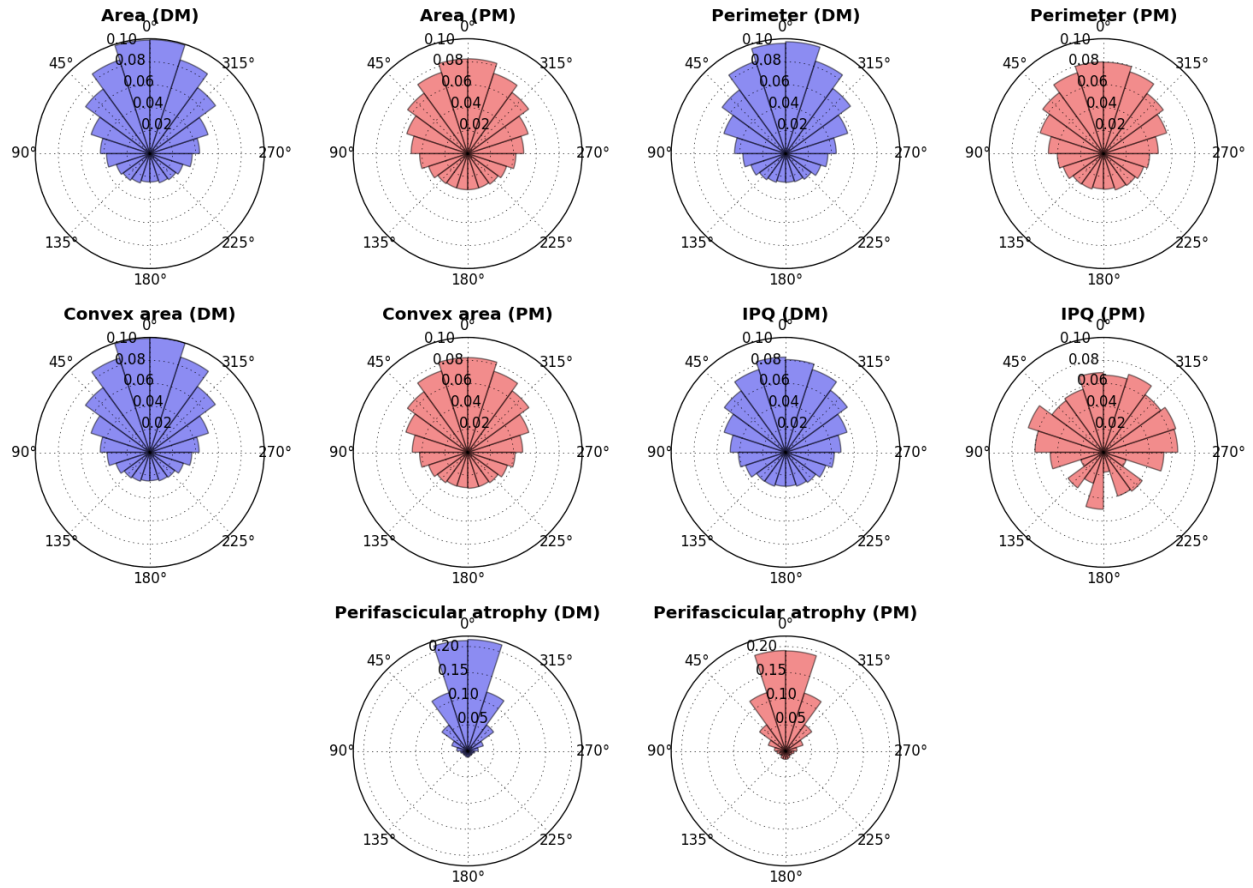
Figure 3-3. Polar histograms of feature gradient variation. The polar histograms formed by measuring the difference in angle of adjacent gradients in the myofiber graph. For each myofiber, the difference in angle of its gradient with respect to the gradients of its neighbors is computed. These polar histograms depict the difference in these gradient angles for several features. Note that in most cases the difference between DM and PM lies in the spread of the histogram around the zero-degree position. The IPQ feature has one of the most distinct polar plots with respect to DM and PM.

CHAPTER 4
DISCUSSION

This study has illustrated that CAD for single-stain analytics of HE-stained muscle biopsies is a viable and robust tool to assist in the diagnosis of myositis. To our knowledge, this is the only muscle study to date that combines morphometric information from muscle fibers with distribution information garnered from nuclei and perimysium to make classification. It is also the only study to attempt classification between forms of myositis using purely image-based computed features. The findings we have presented show that this method, which harnesses segmentation, detection, and informatics techniques to make diagnostic recommendations on muscle tissue, has the potential to be of both clinical and academic significance to researchers of muscle tissue and myositis.

For the most part, the features selected by the confidence interval method confirm the conventional wisdom of myositis diagnosis, most specifically the perifascicular atrophy feature. Of the 19 percentile features derived from perifascicular atrophy measurements in the training data, all but one (gradient angle of perifascicular atrophy 25th percentile) were significant ($p < 0.05$). This study confirms that the size of myofibers, the distance between adjacent myofibers, the distribution of nuclei with respect to myofibers and perimysium, myonuclei count, and even fiber color all bear some predictive significance regarding the diagnosis of myositis. In addition, this study clearly demonstrates that formulations of such features using computer vision techniques have the potential to be powerful tools for computational pathology, whether for describing and analyzing muscle biopsies or for diagnosing myositis.

In order for such a technology to truly shine as a technique for high-throughput analysis of skeletal muscle biopsies, it would need to be fully automated, from input whole slide image to output analytics. As it currently stands, only the perimysium annotation is accomplished manually. Perimysium possesses a nearly identical texture to the endomysium and other connective tissues in muscle biopsies and can vary greatly in its width. Thus, attempts to distinguish perimysium from endomysium at the pixel level using such low-level information are bound to fail. The task of automatic perimysium annotation is a daunting one that requires synthesis of large-scale morphological information and small-scale intensity information to achieve pixel-wise annotation of an entire WSI, whose pixel count is often in the tens of thousands along each dimension. As far as the authors are aware, there exists only one example in the literature of such an algorithm [23]. Incorporation of these perimysium annotation techniques into the segmentation stage could fully automate the process described in this paper. Nonetheless, diagnosis accuracy without using the perimysium features is still quite decent (83.9%) and likely to improve with a larger data set and more features.

This study was limited to slides from only two patient cohorts. Testing this model on additional cohorts obtained using different equipment and staining protocols is necessary to fully establish the generalizability of our method. In fact, retraining the contour detection, hierarchical image segmentation, and nuclei detection stages of our method on cohorts from many different institutions is likely to mitigate the overfitting effect, thereby improving performance on all data sets. We also made the decision to omit IBM cases from our study. IBM is conventionally differentiated by identifying rimmed vacuoles with Gömöri trichrome staining, not by HE staining methods alone.

Additionally, the historic diagnostic criteria for myositis suggested by Bohan and Peter [34], still widely used to analyze muscle WSI in clinical practice, predate the recognition of IBM as a distinct subset of myositis and there is recent evidence to suppose that it may in fact belong to a separate category of myodegenerative disease [2]. For these reasons, IBM was omitted from this study. However, we do not wish to preclude the notion that IBM is possible to diagnose with HE staining and appropriate features. These techniques explored in this paper should be extensible to any type of staining and tissue as long as appropriate disease-specific considerations are made and enough data is present for training.

The WSI patch sampling strategy is another shortcoming of this study. Since the size of our WSI images is typically on the order of hundreds of millions of pixels and occasionally exceeding billions of pixels, applying our segmentation and feature extraction methods on the raw slides is computationally infeasible. To cope with this, we systematically crop regions from each slide in a grid-like fashion. Of these cropped images, we manually remove those that are out of focus, mostly comprised of background, or contain significant amounts of sampling artifacts. A sophisticated sample rejection strategy, such as a trained classifier, could be employed to automatically remove such images in the future. Alternatively, one could also employ an attention-like model to locate regions of interest (ROI) that are of interest to the diagnostic task at hand [35, 36].

Although the focus of our study was on myositis differentiation, the software we have developed has potential application in any setting where the quantitative analysis of skeletal muscle fibers or the immune response within skeletal muscle is of interest.

We envision our combined detection, segmentation, feature extraction, and classification system will pave the way for software that facilitates the analysis, comparison, and diagnosis of myopathy and other diseases of the skeletal muscle. The dystrophin deficiency that lays the foundation of muscular dystrophy, for instance, may afflict the muscle tissue with necrosis and regeneration, myophagocytosis, endomysial inflammation, and fibrosis, all of which may be quantified by the specific feature extractors we have developed [37]. Any myopathy in which inflammation or morphological changes to the myofibers and connective tissue are implicated could possibly be characterized by our features, opening the door for other disease-specific classification tasks to be solved. Additionally, quantification of these morphological changes alone should be of interest to myopathy researchers who wish to analyze muscular abnormalities in a robust way with high throughput. Combined with a content-based image retrieval system, researchers could not only derive insights from their own tissue samples, they could rapidly compare them with similar examples from a database of samples [35, 38, 39].

LIST OF REFERENCES

1. Dorph C, Lundberg IE. Idiopathic inflammatory myopathies--myositis. Best Practice & Research Clinical Rheumatology. 2002;16:817-832.

2. Mammen AL. Autoimmune myopathies: autoantibodies, phenotypes and pathogenesis. Nature Reviews Neurology. 2011;7:343-354.

3. Tanimoto K, Nakano K, Kano S, Mori S, Ueki H, Nishitani H, Sato T, Kiuchi T, Ohashi Y. Classification criteria for polymyositis and dermatomyositis. The Journal of Rheumatology. 1995;22:668-674.

4. Nirmalananthan N, Holton JL, Hanna MG. Is it really myositis? A consideration of the differential diagnosis. Current Opinion in Rheumatology. 2004;16:684-691.

5. Beck AH, Sangoi AR, Leung S, Marinelli RJ, Nielsen TO, van de Vijver MJ, West RB, van de Rijn M, Koller D. Systematic Analysis of Breast Cancer Morphology Uncovers Stromal Features Associated with Survival. Science Translational Medicine. 2011;3:108-113.

6. Andor N, Graham TA, Jansen M, Xia LC, Aktipis CA, Petritsch C, Ji HP, Maley CC. Pan-cancer analysis of the extent and consequences of intratumor heterogeneity. Nature Medicine. 2016;22:105-113.

7. Duff EP, Vennart W, Wise RG, Howard MA, Harris RE, Lee M, Wartolowska K, Wanigasekera V, Wilson FJ, Whitlock M, et al. Learning to identify CNS drug action and efficacy using multistudy fMRI data. Science Translational Medicine. 2015;7:274-16.

8. Quinn SP, Zahid MJ, Durkin JR, Francis RJ, Lo CW, Chennubhotla SC. Automated identification of abnormal respiratory ciliary motion in nasal biopsies. Science Translational Medicine. 2015;7:299-124.

9. Tran PT, Bendapudi PK, Lin HJ, Choi P, Koh S, Chen J, Horng G, Hughes NP, Schwartz LH, Miller VA, et al. Survival and Death Signals Can Predict Tumor Response to Therapy After Oncogene Inactivation. Science Translational Medicine. 2011;3:103-99.

10. Syed Z, Stultz CM, Scirica BM, Guttag JV. Computationally Generated Cardiac Biomarkers for Risk Stratification After Acute Coronary Syndrome. Science Translational Medicine. 2011;3:102-95.

11. Cloonan SM, Glass K, Laucho-Contreras ME, Bhashyam AR, Cervo M, Pabón MA, Konrad C, Polverino F, Siempos II, Perez E, et al. Mitochondrial iron chelation ameliorates cigarette smoke-induced bronchitis and emphysema in mice. Nature Medicine. 2016;22:163-174.

12. Escudero LM, Costa LF, Kicheva A, Briscoe J, Freeman M, Babu MM. Epithelial organisation revealed by a network of cellular contacts. Nature Communications. 2011;2:526.

13. Su H, Xing F, Lee JD, Peterson CA, Yang L. Automatic myonuclear detection in isolated single muscle fibers using robust ellipse fitting and sparse representation. IEEE/ACM Transactions on Computational Biology and Bioinformatics (TCBB). 2014;11:714-726.

14. Liu F, Mackey AL, Srikuea R, Esser KA, Yang L. Automated image segmentation of haematoxylin and eosin stained skeletal muscle cross-sections. Journal of Microscopy. 2013;252:275-285.

15. Liu F, Fry CS, Mula J, Jackson JR, Lee JD, Peterson CA, Yang L. Automated Fiber Type Specific Cross-sectional Area Assessment and Myonuclei Counting in Skeletal Muscle. Journal of Applied Physiology. 2013.

16. Kim YJ, Brox T, Feiden W, Weickert J. Fully automated segmentation and morphometrical analysis of muscle fiber images. Cytometry. 2007;71:8-15.

17. Sáez A, Rivas E, Montero-Sánchez A, Paradas C, Acha B, Pascual A, Serrano C, Escudero LM. Quantifiable diagnosis of muscular dystrophies and neurogenic atrophies through network analysis. BMC Medicine. 2013;11:77.

18. Meunier B, Picard B, Astruc T, Labas R. Development of image analysis tool for the classification of muscle fibre type using immunohistochemical staining. Histochemistry and Cell Biology. 2010;134:307-317.

19. Karen P, Števanec M, Smerdu V, Cvetko E, Kubínová L, Eržen I. Software for muscle fibre type classification and analysis. European Journal of Histochemistry. 2009;53:2-11.

20. Garton F, Seto JT, North KN, Yang N. Validation of an automated computational method for skeletal muscle fibre morphometry analysis. Neuromuscular Disorders. 2010;20:540-547.

21. Liu F, Xing F, Zhang Z, McGough M, Yang L. Robust Muscle Cell Quantification Using Structured Edge Detection and Hierarchical Segmentation. Medical Image Computing and Computer-Assisted Intervention. 2015;9351:324-331.

22. Xie Y, Xing F, Kong X, Su H, Yang L. Beyond Classification: Structured Regression for Robust Cell Detection Using Convolutional Neural Network. Medical Image Computing and Computer-Assisted Intervention. 2015;9351:358-365.

23. Sapkota M, Xing F, Su H, Yang L. Automatic muscle perimysium annotation using deep convolutional neural network. IEEE 12th International Symposium on Biomedical Imaging. 2015;205-208.

24. Lin M, Lucas Jr HC, Shmueli G. Research Commentary-Too Big to Fail: Large Samples and the p-Value Problem. Information Systems Research. 2013;24:906-917.

25. Arbelaez P, Maire M, Fowlkes C, Malik J. Contour Detection and Hierarchical Image Segmentation. IEEE Transactions on Pattern Analysis and Machine Intelligence. 2011;33:898-916.

26. Veta M, van Diest PJ, Willems SM, Wang H, Madabhushi A, Cruz-Roa A, Gonzalez F, Larsen AB, Vestergaard JS, Dahl AB, et al. Assessment of algorithms for mitosis detection in breast cancer histopathology images. Medical Image Analysis. 2015;20:237-248.

27. Girshick R, Donahue J, Darrell T, Malik J. Rich Feature Hierarchies for Accurate Object Detection and Semantic Segmentation. Proceedings of the IEEE Conference on Computer Vision and Pattern Recognition. 2014;580-587.

28. Cireşan DC, Giusti A, Gambardella LM, Schmidhuber J. Mitosis Detection in Breast Cancer Histology Images with Deep Neural Networks. International Conference on Medical Image Computing and Computer-Assisted Intervention. 2013;411-418

29. Xie W, Noble JA, Zisserman A. Microscopy Cell Counting with Fully Convolutional Regression Networks. International Conference on Medical Image Computing and Computer-Assisted Intervention. 2015;

30. Giusti A, Cireşan DC, Masci J, Gambardella LM, Schmidhuber J. Fast Image Scanning with Deep Max-Pooling Convolutional Neural Networks. arXiv:1302.1700. 2013.

31. Dalakas MC, Hohlfeld R. Polymyositis and dermatomyositis. The Lancet. 2003;9388:971-982.

32. Van Ginneken B, Frangi AF, Staal JJ, ter Haar Romeny BM, Viergever MA. Active shape model segmentation with optimal features. IEEE Transactions on Medical Imaging. 2002;21:924-933.

33. Selva OA, Trallero AE. Inflammatory myopathies. Dermatomyositis, polymyositis, and inclusion body myositis. Reumatologia Clinica. 2008;4:197-206.

34. Bohan A, Peter JB. Polymyositis and Dermatomyositis. New England Journal of Medicine. 1975;292:403-407.

35. Liu GH, Yang JY, Li Z. Content-based image retrieval using computational visual attention model. Pattern Recognition. 2015;48;2554-2566.

36. Xu K, Ba J, Kiros R, Cho K, Courville A, Salakhutdinov R, Zemel R, Bengio Y. Show, Attend and Tell: Neural Image Caption Generation with Visual Attention. arXiv:1502.03044. 2015.

37. Rosenberg AS, Puig M, Nagaraju K, Hoffman EP, Villalta SA, Rao VA, Wakefield LM, Woodcock J. Immune-mediated pathology in Duchenne muscular dystrophy. Science Translational Medicine. 2015;299:299.

38. Wei L, Bo L, Peng C, Jinzhu Y. Combining Text and Content Based Image Retrieval on Medical Resource Database. 2013; DOI: 10.2991/icmt-13.2013.215

39. Kumar A, Kim J, Cai W, Fulham M, Feng D. Content-Based Medical Image Retrieval: A Survey of Applications to Multidimensional and Multimodality Data. Journal of Digital Imaging. 2013;26:1025-1039.

BIOGRAPHICAL SKETCH

Mason majored in biomedical engineering, graduating with a Master of Science degree in the fall of 2016. During his studies, he volunteered and eventually worked a part-time position for the J. Crayton Pruitt Family Department of Biomedical Engineering.